

# Numerical modeling of collisional dynamics of Sr in an optical dipole trap

M. Yan, R. Chakraborty, P. G. Mickelson, Y. N. Martinez de Escobar, and T. C. Killian  
*Rice University, Department of Physics and Astronomy, Houston, Texas, 77251*

(Dated: February 6, 2020)

We describe a model of inelastic and elastic collisional dynamics of atoms in an optical dipole trap that utilizes numerical evaluation of statistical mechanical quantities and numerical solution of equations for the evolution of number and temperature of trapped atoms. It can be used for traps that possess little spatial symmetry and when the ratio of trap depth to sample temperature is relatively small. We check parameters calculated numerically against analytic calculations for power-law traps and compare results with experiments on  $^{88}\text{Sr}$ , which has well-characterized collisional properties.

## I. INTRODUCTION

Understanding the collisional dynamics of trapped, ultracold atoms is essential for optimizing forced evaporative cooling [1, 2] and obtaining quantum degenerate Bose [3] and Fermi gases [4]. It also allows determination of ultracold collision properties from the evolution of number and temperature in a trapped sample of atoms or molecules [5, 6, 7].

Many recipes have been presented for relating the evolution of the trapped gas to underlying physical parameters. Typically the collisional dynamics are described by differential equations for the time rate of change of the atom number  $N$  and total energy  $E$ , as originally suggested by [1, 2]. The method has been extended and developed in many other works [8, 9, 10, 11, 12, 13, 14, 15]. The standard treatment of evaporation is described by Luiten *et al.* [10], which derives expressions for thermodynamic quantities from the kinetic equations using an assumption of sufficient ergodicity and a truncated Boltzmann velocity distribution. Analytic evaluation of these expressions is straightforward for power-law traps. Noteworthy subsequent improvements over this work include the addition of effects of time-dependent potentials [11], energy-dependent cross sections [12], and quantum statistics [13]. Prescriptions have been offered for optimizing evaporation [14] and deriving scaling laws [15]. Direct Monte Carlo simulations have also been presented to relax the assumption of sufficient ergodicity [16] and treat hydrodynamic effects [17].

A common simplifying assumption is that  $\eta$ , the ratio of trap depth  $\epsilon_t$  to sample temperature  $k_B T$  with Boltzmann constant  $k_B$ , is large. For example, this yields analytic expressions for thermodynamic quantities, and allows approximation of optical dipole traps [18] as parabolic potentials [19]. By taking advantage of the high degree of spatial symmetry in a linear potential, analytic expressions for thermodynamic quantities were derived for the low- $\eta$  situation ( $\eta < 4$ ) in this particular geometry [20]. It is worth emphasizing that Luiten's model [10] is, in principle, valid for low  $\eta$ , as long as the assumptions of ergodicity and a truncated Boltzmann distribution are also valid.

If the potential lacks the ideal shape of a power-law

trap, simple analytic expressions for many quantities of interest cannot be found, and numerical methods are required. This is the case for low- $\eta$  in an optical dipole trap and especially when gravity is significant.  $^{88}\text{Sr}$  in an optical dipole trap falls into this situation because of its large mass and extremely small  $s$ -wave scattering length  $a = -1.4(6)a_0$  [21], where the Bohr radius  $a_0 = 5.3 \times 10^{-11}\text{m}$ . In the present work, we present numerical methods for describing collisional dynamics in a static trap in this regime, based on the works of Luiten *et al.* [10] and Comparat *et al.* [19], and apply them to describe experiments with  $^{88}\text{Sr}$ .

This paper is organized as follows. Section II describes the experimental setup, and then section III presents the collisional processes important in the trapped sample and the differential equations for evolution of  $N$  and  $E$ . As a check of numerics, and to study ranges of validity of various approximations, a comparison of numerical calculations with corresponding analytic results for power-law traps is presented in section IV. A brief introduction to the numerical code, as applied to trapped  $^{88}\text{Sr}$ , is provided in section V. Finally, the elastic collision cross section of  $^{88}\text{Sr}$  inferred from the fit of the numerical model to observations is compared with theoretical results in section VI.

## II. EXPERIMENTAL SETUP

The creation of samples of  $^{88}\text{Sr}$  atoms in an optical dipole trap (ODT) starts with laser cooling and trapping phases that have been described in detail previously [22, 23, 24]. Atoms are trapped in a magneto-optical trap (MOT) operating on the 461 nm  $^1S_0$ - $^1P_1$  transition (Fig. 1) and cooled to about 2 mK. There is a decay channel from the  $^1P_1$  state, to the  $^1D_2$  state with a branching ratio of  $2 \times 10^{-5}$ . This can subsequently populate the metastable  $^3P_2$  level.  $^3P_2$  atoms are repumped by applying a 3  $\mu\text{m}$  laser resonant with the  $^3P_2$ - $^3D_2$  transition that returns these atoms to the ground state. The repumped sample of atoms contains about  $3.5 \times 10^8$  atoms.

After this initial MOT stage, the 461 nm light is extinguished and the atom sample is transferred with more than 50% efficiency to a second MOT operating on the  $^1S_0$ - $^3P_1$  intercombination line [25]. The sample is cooled

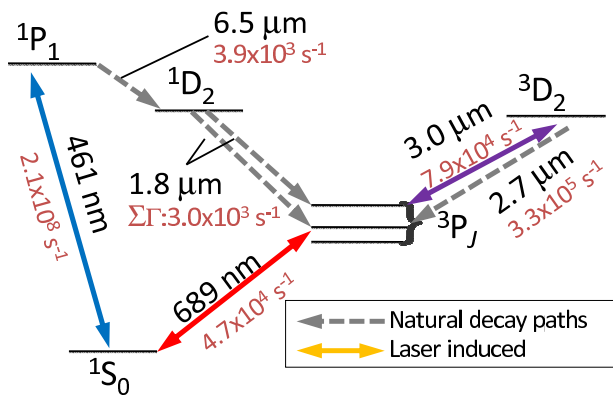


FIG. 1: (Color online) Atomic Sr energy levels involved in the two-photon PAS experiments. Decay rates ( $\text{s}^{-1}$ ) and excitation wavelengths are given for selected transitions. Laser light used for the experiment is indicated by solid lines. Atoms decaying to the  $^3P_2$  level may be repumped by  $3 \mu\text{m}$  light.

to  $3 \mu\text{K}$ , producing densities of  $10^{12} \text{ cm}^{-3}$ .

Atoms are then transferred to an ODT generated from a 21 W, 1064 nm, linearly-polarized, single-transverse-mode fiber laser. The experimental setup in this work is shown in Fig. 2. The trap is in a crossed-beam configuration, derived from the first order deflection of an acousto-optic modulator. The beam is focused on the atoms with a minimum  $e^{-2}$  intensity-radius of  $w \approx 100 \mu\text{m}$ . It is then reflected back through the chamber to intersect the first beam at 90 degrees and refocused to have approximately the same waist at the atoms. Both beams lie in a plane that is inclined  $10.5^\circ$  from horizontal.

The number of atoms and sample temperature are determined with time-of-flight absorption imaging using the  $1S_0-1P_1$  transition. The ODT trapping potential is calculated from measured laser beam parameters and the polarizability of the  $1S_0$  state [26], and it is checked by measuring the trap oscillation frequencies through the parametric resonance technique [27]. This allows us to infer the sample density profile from the temperature and number of trapped atoms.

### III. MODEL OF COLLISIONAL DYNAMICS

The evolution of  $N$  and  $E$  is described by a system of differential equations. Different terms in the equations represent physical processes such as elastic and inelastic collisions, and processes involving laser fields.

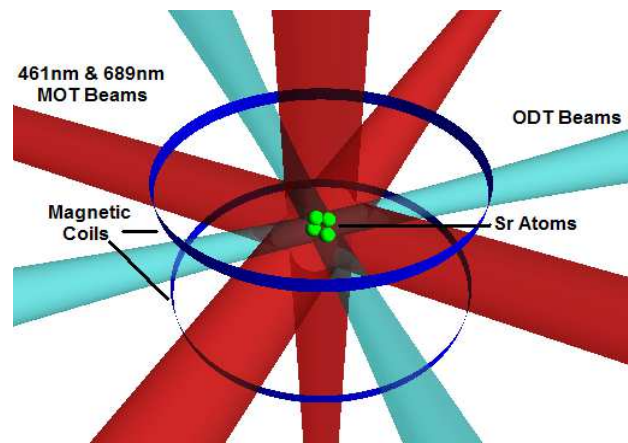


FIG. 2: (Color Online) Schematic of our experiment illustrating the overlap of ODT beams with MOT beams and relative positions of magnetic coils.

#### A. Description of Basic Processes

##### 1. Background collisions and inelastic collisional losses

One-body losses due to collisions with background gas and two- and three-body inelastic collisional losses are described by the local equation

$$\dot{n} = -\Gamma_{bg}n - \beta_{in}n^2 - Ln^3, \quad (1)$$

where  $n$  is the atomic density. In simulations described here, we will assume that the loss rate constants  $\Gamma_{bg}$ ,  $\beta_{in}$ , and  $L$  are independent of temperature. Integrating Eq. 1 over the trap volume gives

$$\dot{N} = -(\Gamma_{bg} + \beta_{in}N \frac{V_2}{V_1} + LN^2 \frac{V_3}{V_1^3})N, \quad (2)$$

where the effective volumes are

$$V_q \equiv \frac{1}{n_{peak}^q} \int d^3r [n(\mathbf{r})]^q. \quad (3)$$

We have also made use of the relationship between peak density and total number,  $n_{peak}V_1 = N$ .

The energy or temperature evolution due to these processes for a constant trap potential can be found as follows. The rate of energy change in an infinitesimal volume  $dV$  is

$$d\dot{E} = -\dot{n}(\mathbf{r})dV(U(\mathbf{r}) + \bar{E}_k(\mathbf{r})), \quad (4)$$

where  $U(\mathbf{r})$  is the trap potential and  $\bar{E}_k(\mathbf{r})$  is the average kinetic energy per atom located at  $\mathbf{r}$ .  $U(\mathbf{r})$  is defined to have a value of  $U = 0$  at the trap minimum. We assume a truncated Boltzmann phase-space distribution (this is valid if the trap is sufficiently ergodic [10]), which implies that the kinetic energy in a given differential volume also obeys a truncated Boltzmann distribution truncated at

the kinetic energy required for an atom to escape the trap from the differential volume. Thus the position-dependent average kinetic energy can be expressed as

$$\bar{E}_k(\mathbf{r}) = \frac{\int_0^{\epsilon_t - U(\mathbf{r})} dE_k E_k^{3/2} e^{-E_k/k_B T}}{\int_0^{\epsilon_t - U(\mathbf{r})} dE_k E_k^{1/2} e^{-E_k/k_B T}}. \quad (5)$$

Integrating Eq. 4 yields the rate of change of total energy

$$\begin{aligned} \dot{E} = & -\Gamma_{bg} \left( \frac{T_1 + P_1}{V_1} \right) N - \beta_{in} \left( \frac{T_2 + P_2}{V_1^2} \right) N^2 \\ & - L \left( \frac{T_3 + P_3}{V_1^3} \right) N^3. \end{aligned} \quad (6)$$

We have introduced the effective kinetic energies

$$T_q \equiv \frac{1}{n_{peak}^q} \int d^3 r [n(\mathbf{r})]^q \bar{E}_k(\mathbf{r}), \quad (7)$$

and effective potential energies

$$P_q \equiv \frac{1}{n_{peak}^q} \int d^3 r [n(\mathbf{r})]^q U(\mathbf{r}). \quad (8)$$

Note that the total energy of atoms inside the trap is  $E = (T_1 + P_1) \frac{N}{V_1}$ . In the high- $\eta$  limit,  $\bar{E}_k(\mathbf{r}) = \frac{3}{2} k_B T$ , which can be taken out of the integrals to yield

$$\begin{aligned} \dot{E} \approx & -\frac{3}{2} k_B T \left( \Gamma_{bg} N + \beta_{in} \frac{V_2}{V_1^2} N^2 + L \frac{V_3}{V_1^3} N^3 \right) \\ & - \left( \Gamma_{bg} \frac{P_1}{V_1} N + \beta_{in} \frac{P_2}{V_1^2} N^2 + L \frac{P_3}{V_1^3} N^3 \right). \end{aligned} \quad (9)$$

## 2. Off-resonant laser scattering

The scattering of off-resonant photons, such as from the ODT laser, heats the atoms due to momentum diffusion (MD) [28]. The rate of change of total energy due to this process is

$$\dot{E}_{MD} = \Gamma_{laser} N E_{recoil}, \quad (10)$$

where the total scattering rate of light from the laser field is given by  $\Gamma_{laser}$ . If the light scattering rate is dominated by one transition,  $\Gamma_{laser} = \frac{s_0 \gamma / 2}{1 + s_0 + (2\delta/\gamma)^2}$ , in which  $s_0$  is the saturation parameter,  $\delta$  is the detuning of the laser, and  $\gamma$  is the linewidth of the transition. The recoil energy is  $E_{recoil} = k_B T_{recoil} = \hbar^2 k^2 / m$  where  $\hbar$  is Planck's constant  $h$  divided by  $2\pi$ ,  $k$  is the photon circular wavenumber, and  $m$  is the atom mass.

## 3. Evaporation

To describe the rate of atom loss due to evaporation, we follow the treatment of [10], which assumes ergodicity

and a truncated Boltzmann distribution,

$$\begin{aligned} f(\mathbf{r}, \mathbf{p}) = & \frac{n_0}{(2\pi m k_B T)^{3/2}} \exp[-(U(\mathbf{r}) + p^2/2m)/k_B T] \\ & \times \Theta(\epsilon_t - U(\mathbf{r}) - p^2/2m), \end{aligned} \quad (11)$$

where  $n_0$  is the peak density (the density at the trap minimum) in an infinitely deep trap,  $\Theta(x)$  is the Heaviside step function, and  $p$  is the atom momentum. This yields a density distribution given by

$$\begin{aligned} n(\mathbf{r}) = & n_{peak} A e^{-U(\mathbf{r})/k_B T} \left\{ \text{erf} \left[ \sqrt{\frac{\epsilon_t - U(\mathbf{r})}{k_B T}} \right] \right. \\ & \left. - 2 \sqrt{\frac{\epsilon_t - U(\mathbf{r})}{\pi k_B T}} \exp \left[ -\frac{\epsilon_t - U(\mathbf{r})}{k_B T} \right] \right\}, \end{aligned} \quad (12)$$

where the normalization constant  $A$  is given by

$$A = \frac{n_0}{n_{peak}} = \left\{ \text{erf} \left[ \sqrt{\frac{\epsilon_t}{k_B T}} \right] - 2 \sqrt{\frac{\epsilon_t}{\pi k_B T}} \exp \left[ -\frac{\epsilon_t}{k_B T} \right] \right\}^{-1}. \quad (13)$$

It is important to note that  $n_0$  is no longer the peak density since the peak density is redefined as

$$\begin{aligned} n_{peak} = & n(\mathbf{r})|_{U(\mathbf{r})=0} \\ = & n_0 \left\{ \text{erf} \left[ \sqrt{\epsilon_t/k_B T} \right] \right. \\ & \left. - 2 \sqrt{\epsilon_t/\pi k_B T} \exp \left[ -\epsilon_t/k_B T \right] \right\}. \end{aligned} \quad (14)$$

The total number of atoms lost per unit time due to evaporation can then be written as

$$\dot{N}_{ev} = -\Gamma_{ev} N, \quad (15)$$

where the evaporation rate per atom is

$$\Gamma_{ev} = \frac{N}{V_1^2} A^2 \sigma_{el} \bar{v} e^{-\eta} V_{ev}. \quad (16)$$

Here,  $\sigma_{el}$  is the elastic collision cross section, which is assumed to be collision-energy independent in this treatment.  $\bar{v} = \left( \frac{8k_B T}{\pi m} \right)^{1/2}$  is the mean atomic velocity, and the effective volume for elastic collisions leading to evaporation is

$$V_{ev} = \frac{\Lambda^3}{k_B T} \int_0^{\epsilon_t} d\epsilon \rho(\epsilon) [(\epsilon_t - \epsilon - k_B T) e^{-\epsilon/k_B T} + k_B T e^{-\eta}], \quad (17)$$

where

$$\Lambda = (2\pi \hbar^2 / m k_B T)^{1/2} \quad (18)$$

is the thermal de Broglie wavelength. The density of states in the trap is given by

$$\rho(\epsilon) = \frac{2\pi(2m)^{3/2}}{h^3} \int_{U(\mathbf{r}) \leq \epsilon_t} d^3 r \sqrt{\epsilon - U(\mathbf{r})}. \quad (19)$$

Similarly, the rate of change of total energy due to evaporation is

$$\dot{E}_{ev} = -\Gamma_{ev}N\bar{E}_{ev}, \quad (20)$$

where the average energy loss per evaporated atom is

$$\bar{E}_{ev} = \epsilon_t + \frac{V_{ev} - X_{ev}}{V_{ev}}k_B T, \quad (21)$$

with

$$X_{ev} = \frac{\Lambda^3}{k_B T} \int_0^{\epsilon_t} d\epsilon \rho(\epsilon) [k_B T e^{-\epsilon/k_B T} - (\epsilon_t - \epsilon + k_B T) e^{-\eta}]. \quad (22)$$

#### 4. Final equations

Accounting for all processes, the equations for number and energy evolution become

$$\begin{aligned} \dot{N} = & -\Gamma_{bg}N - \frac{1}{V_1^2}(\beta_{in}V_2 + A^2\sigma_{el}\bar{v}e^{-\eta}V_{ev})N^2 \\ & -L\frac{V_3}{V_1^3}N^3, \end{aligned} \quad (23)$$

$$\begin{aligned} \dot{E} = & -\Gamma_{bg}\left(\frac{T_1 + P_1}{V_1}\right)N - \beta_{in}\left(\frac{T_2 + P_2}{V_1^2}\right)N^2 \\ & -L\left(\frac{T_3 + P_3}{V_1^3}\right)N^3 + \Gamma_{laser}NE_{recoil} \\ & -\frac{N^2}{V_1^2}A^2\sigma_{el}\bar{v}e^{-\eta}V_{ev}\left[\epsilon_t + \frac{V_{ev} - X_{ev}}{V_{ev}}k_B T\right]. \end{aligned} \quad (24)$$

#### B. Ratio of Elastic to Inelastic Cross Sections

For interpretation of some experimental data, it is necessary to calculate additional factors that describe the roles of inelastic and elastic two-body collisions. As pointed out in [20], losses due to inelastic two-body collisions and evaporation both scale with the number or density of atoms squared, which makes it difficult to measure the rates of the two processes individually from loss curves alone. Additional measurements of temperature, along with a statistical mechanical model of evaporation and inelastic loss in the trap can overcome this problem.

When all loss processes except evaporation and two-body inelastic collisions are negligible, because inelastic loss is a heating mechanism and evaporation is a cooling mechanism, the atoms tend toward a steady state temperature that is independent of the number of atoms in the trap [20]. The ratio of trap depth to the steady state temperature is the equilibrium  $\eta$  (at constant trap depth). Assuming that the steady state temperature is reached, the local loss equation is  $\dot{n} = -\beta n^2$  where  $\beta$  is the total two-body loss rate constant (including inelastic and evaporative losses)  $\beta = \beta_{in} + f(\eta)\beta_{el}$ , where  $f(\eta)$  is the fraction of an atom's elastic collisions that result

in the evaporation of that atom [31], and  $\beta_{in/el}$  are the inelastic and elastic collision rate constants. For an untruncated Boltzmann (or very large  $\eta$ )  $\beta_{el} = \sqrt{2}\sigma_{el}\bar{v}$ , where  $\bar{v} = \sqrt{\frac{8k_B T}{\pi m}}$ . Typically,  $\beta_{in} \equiv 2K$ , where  $K$  is the inelastic collision event rate constant, each collision results in the loss of both atoms, and  $\beta_{in} = \sqrt{2}\sigma_{in}\bar{v}$ . The relative contributions of inelastic and elastic losses can be described by [20]

$$\beta_{in} = \frac{1}{f\gamma + 1}\beta, \quad (25)$$

$$\beta_{el} = \frac{\gamma}{f\gamma + 1}\beta, \quad (26)$$

where the ratio of elastic to inelastic cross sections is

$$\gamma \equiv \frac{\beta_{el}}{\beta_{in}} = \frac{\sigma_{el}}{\sigma_{in}} = \frac{\bar{E} - \bar{E}_d}{f(\bar{E}_{ev} - \bar{E})}, \quad (27)$$

and  $\bar{E} = (T_1 + P_1)/V_1$  is the average energy of the trapped atoms,  $\bar{E}_d = (T_2 + P_2)/V_2$  is the average energy of atoms lost due to inelastic collisions, and  $\bar{E}_{ev}$  is the average energy of atoms lost due to evaporation (Eq. 21). All variables on the right-hand side depend only on  $\eta$ , which is constant at equilibrium.

The calculation of  $f$  is somewhat involved. It is given in terms of other collisional parameters by

$$f(\eta) = \frac{\Gamma_{ev}}{\Gamma_{el}}, \quad (28)$$

where  $\Gamma_{ev}$  is the evaporation rate per atom (Eq. 16) and  $\Gamma_{el}$  is the elastic collision rate per atom (number of collisions per second, on average, that an atom in the trap suffers). Several ancillary quantities must be calculated in order to find  $\Gamma_{el}$ . The number of elastic collisions per second per unit volume at position  $\mathbf{r}$  is [29, 30]

$$Z(\mathbf{r}) = \frac{1}{2} \int d^3 p_1 \int d^3 p_2 \sigma_{el} |\mathbf{v}_1 - \mathbf{v}_2| f(\mathbf{r}, \mathbf{p}_1, t) f(\mathbf{r}, \mathbf{p}_2, t), \quad (29)$$

where  $\mathbf{v}_1 = \mathbf{p}_1/m$ ,  $\mathbf{v}_2 = \mathbf{p}_2/m$ , and we have assumed an energy-independent elastic cross section. For a truncated Boltzmann distribution independent of time, this integral must be evaluated numerically. In the large- $\eta$  limit, it reduces to the standard result

$$Z(U(\mathbf{r})) = 2\sigma_{el}[n(\mathbf{r})]^2 \sqrt{\frac{k_B T}{\pi m}}. \quad (30)$$

The total number of elastic collisions happening per second inside the trap can be found by integrating  $Z$  over the volume of the trap. There are two atoms involved in every collision. So the average rate at which an atom undergoes elastic collisions in the trap is

$$\Gamma_{el} = \frac{2}{N} \int d^3 r Z(U(\mathbf{r})), \quad (31)$$

and  $f\Gamma_{el}N$  is the number of evaporating atoms per second. For an untruncated Boltzmann distribution,  $\Gamma_{el}$  in a square, a parabolic, and a linear potential are  $\sqrt{2}n_0\sigma_{el}\bar{v}$ ,  $n_0\sigma_{el}\bar{v}/2$ , and  $n_0\sigma_{el}\bar{v}/4\sqrt{2}$  respectively [20].

#### IV. CHECK OF NUMERICAL QUANTITIES

In principle, all the quantities necessary to solve Eqs. 23 and 24 and model collisional dynamics can be calculated, but in practice approximations are necessary to arrive at analytic results. This is straightforward for high- $\eta$  conditions [9], and also in situations of low- $\eta$  and with sufficient trap symmetry [20]. For low- $\eta$  conditions and traps that lack spatial symmetry, numerical evaluation of statistical mechanical quantities is the only option, and that is the approach we follow.

To provide a check of our numerical evaluations, we compare numerical results (numeric, general (NG)) with analytic forms for power-law traps. For the NG spatial integrals for  $\rho(\epsilon)$ ,  $V_q$ ,  $T_q$ , and  $P_q$ , the integration extends over the region in the trap determined from an algorithm that finds the saddle points of the potential. An interpolating function representing  $\rho(\epsilon)$  is used in evaluation of  $V_{ev}$  and  $X_{ev}$  in integrals over an energy interval from 0 to  $\epsilon_t$ . An adaptive-step-size integration routine in *Mathematica* is used to evaluate these integrals.

We use two different analytic forms, one in which the standard high- $\eta$  approximations are used (analytic, high- $\eta$  (AH- $\eta$ )) [9, 20] and one in which the high- $\eta$  approximation is not made and a truncated Boltzmann distribution is assumed (analytic, general (AG)) [10].

##### A. Power-Law Traps

Ideal power-law (PL) trap potentials have the form

$$U(r) = \epsilon_t \left( \frac{r}{R_0} \right)^\gamma. \quad (32)$$

For the linear and parabolic traps  $\gamma = 1$  and  $\gamma = 2$  respectively. The square potential can be viewed as a  $\gamma \rightarrow \infty$  limit

$$U(r)^{Square} = \begin{cases} \infty, & \text{for } r \geq R_0 \\ 0, & \text{for } 0 < r < R_0 \end{cases}. \quad (33)$$

Here,  $\epsilon_t$  and  $R_0$  can be interpreted as scaling parameters. Truncated traps, which lead to truncated Boltzmann distributions, can be expressed as

$$U(r) = \epsilon_t \left( \frac{r}{R_0} \right)^\gamma \Theta(R_0 - r), \quad (34)$$

and

$$U(r)^{Square} = \begin{cases} \epsilon_t, & \text{for } r \geq R_0 \\ 0, & \text{for } 0 < r < R_0 \end{cases}, \quad (35)$$

where  $U(R_0) = \epsilon_t$  is the trap depth and  $R_0$  is the boundary.

##### B. Effective Volumes $V_q$

Effective volumes  $V_q$  are defined in Eq. 3. From the expressions for  $n(\mathbf{r})$  and  $n_{peak}$  given in Eqs. 12-14, the AG form of Eq. 3 can be evaluated exactly as:

$$V_q^{AG} = \frac{4\pi}{[P(\eta, 3/2)]^q} \int_0^{R_0} r^2 e^{-qU(r)/k_B T} \times \left[ P\left(\eta - \frac{U(r)}{k_B T}, \frac{3}{2}\right) \right]^q dr, \quad (36)$$

with the incomplete Gamma function

$$P(\eta, a) = \frac{\int_0^\eta t^{a-1} e^{-t} dt}{\int_0^\infty t^{a-1} e^{-t} dt}. \quad (37)$$

The denominator in Eq. 37 is the Gamma function  $\Gamma(a)$ .

Transforming to the unitless variables  $\tilde{r} = \frac{r}{R_0}$  and  $\frac{U(r)}{k_B T} = \eta \tilde{r}^\gamma$  yields

$$V_q^{AG}(\gamma) = 4\pi R_0^3 \int_0^1 \tilde{r}^2 e^{-q\eta \tilde{r}^\gamma} \times \frac{[P(\eta - \eta \tilde{r}^\gamma, 3/2)]^q}{[P(\eta, 3/2)]^q} d\tilde{r}. \quad (38)$$

If we assume large  $\eta$ , the incomplete gamma function  $P$  tends to unity, and we arrive at the AH- $\eta$  approximation for Eq. 38

$$\begin{aligned} V_q^{AH-\eta}(\gamma) &= 4\pi R_0^3 \int_0^1 \tilde{r}^2 e^{-q\eta \tilde{r}^\gamma} d\tilde{r} \\ &= \frac{4\pi R_0^3}{3} \frac{\Gamma(3/\gamma + 1) - (3/\gamma)\Gamma(3/\gamma, q\eta)}{(q\eta)^{3/\gamma}} \\ &\approx \frac{4\pi R_0^3}{3} \frac{\Gamma(3/\gamma + 1)}{(q\eta)^{3/\gamma}} \\ &= \frac{4\pi R_0^3}{3} \left( \frac{k_B T}{q\epsilon_t} \right)^{3/\gamma} \Gamma(3/\gamma + 1), \end{aligned} \quad (39)$$

where the approximation step takes the limit of the upper incomplete gamma function  $\Gamma(s, \eta) = \int_\eta^\infty t^{s-1} e^{-t} dt \rightarrow 0$  when  $\eta$  is large.

Fig. 3 shows comparison plots of  $V_1$ , scaled by  $V_0 = 4\pi R_0^3/3$ . The NG curves are identical to the AG ones as expected. The high- $\eta$  model is a reasonable approximation for  $\eta \gtrsim 4$  in agreement with [20].

##### C. Effective Volume for Elastic Collisions Leading to Evaporation $V_{ev}$

Effective volumes for elastic collisions leading to evaporation,  $V_{ev}$ , for PL traps in the AG treatment are defined in Eq. 42a in [10]

$$V_{ev}^{AG} = \Lambda^3 \zeta_\infty [\eta P(\eta, 3/2 + 3/\gamma) - (5/2 + 3/\gamma) P(\eta, 5/2 + 3/\gamma)], \quad (40)$$

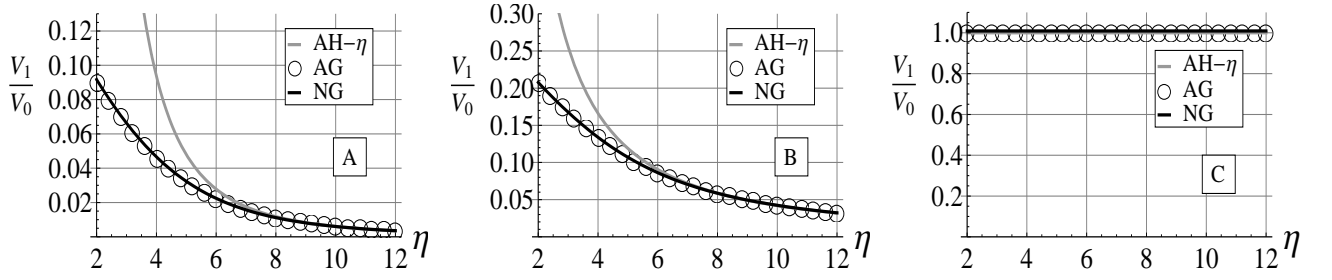


FIG. 3: Plots of  $V_1$  vs  $\eta$  for (A) Linear, (B) Parabolic, and (C) Square potentials.

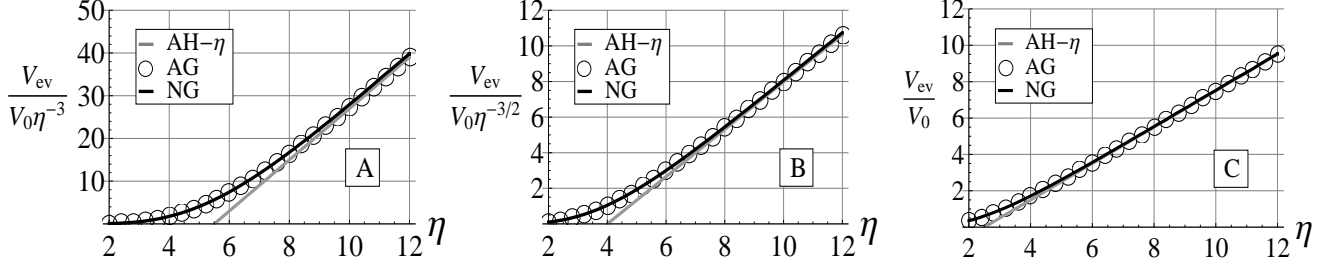


FIG. 4: Plots of  $V_{ev}$  vs  $\eta$  for (A) Linear, (B) Parabolic, and (C) Square potentials.

where the thermal de Broglie wavelength  $\Lambda$  is defined in Eq. 18, and

$$\zeta_\infty = A_{\text{PL}} \Gamma(3/2 + 3/\gamma) (k_B T)^{3/2 + 3/\gamma}. \quad (41)$$

$A_{\text{PL}}$  for PL traps can be expressed by

$$A_{\text{PL}} = \left( \frac{m}{2\pi\hbar^2} \right)^{3/2} \frac{V_0}{(\eta k_B T)^{3/\gamma}} \frac{\Gamma(3/\gamma + 1)}{\Gamma(3/2 + 3/\gamma)}. \quad (42)$$

Accordingly, Eq. 40 can be rewritten as

$$V_{ev}^{AG}(\gamma) = V_0 \eta^{-3/\gamma} \Gamma(3/\gamma + 1) [\eta P(\eta, 3/2 + 3/\gamma) - (5/2 + 3/\gamma) P(\eta, 5/2 + 3/\gamma)]. \quad (43)$$

Because  $P$  tends to unity at high- $\eta$ , the AH- $\eta$  approximation for Eq. 43 is

$$V_{ev}^{AH-\eta}(\gamma) = V_0 \eta^{-3/\gamma} \Gamma(3/\gamma + 1) [\eta - (5/2 + 3/\gamma)]. \quad (44)$$

Comparisons plots of  $V_{ev}$ , scaled by  $V_0 \eta^{-3/\gamma}$  are presented in Fig. 4. The NG and AG curves are identical as expected.

#### D. $X_{ev}$

The volume parameter  $X_{ev}$  (Eq. 22) for PL traps in the AG model is given by

$$X_{ev}^{AG} = \Lambda^3 \zeta_\infty P(\eta, 7/2 + 3/\gamma), \quad (45)$$

which can be written as

$$X_{ev}^{AG}(\gamma) = V_0 \eta^{-3/\gamma} \Gamma(3/\gamma + 1) P(\eta, 7/2 + 3/\gamma). \quad (46)$$

When  $\eta$  is high, this becomes

$$X_{ev}^{AH-\eta}(\gamma) = V_0 \eta^{-3/\gamma} \Gamma(3/\gamma + 1). \quad (47)$$

Comparisons of  $X_{ev}$ , scaled by  $V_0 \eta^{-3/\gamma}$  are plotted in Fig. 5. The agreement between the NG and AG curves is excellent. However, in Fig. 5 (A), (B) and (C), the AH- $\eta$  curves match the AG ones for  $\eta \gtrsim 10$ ,  $\eta \gtrsim 8$  and  $\eta \gtrsim 6$  respectively.

#### E. Evaporation Rate Per Atom $\Gamma_{ev}$

The evaporation rate per atom  $\Gamma_{ev}$  is defined in Eq. 16

$$\Gamma_{ev} = \frac{N}{V_1^2} A^2 \sigma_{el} \bar{v} e^{-\eta} V_{ev} = \frac{n_0}{V_1} A \sigma_{el} \bar{v} e^{-\eta} V_{ev}. \quad (48)$$

Eq. 48 in the AG model can be evaluated exactly as

$$\Gamma_{ev}^{AG} = \frac{n_0}{V_1^{AG}} A \sigma_{el} \bar{v} e^{-\eta} V_{ev}^{AG}, \quad (49)$$

with  $V_1^{AG}$  and  $V_{ev}^{AG}$  given by Eqs. 38 and 43 respectively.

In the high- $\eta$  approximation, the normalization constant  $A$  and the incomplete gamma function  $P$  both tend to unity. Substituting  $V_1^{AH-\eta}$  and  $V_{ev}^{AH-\eta}$  from Eq. 39 and Eq. 44 into Eq. 48 yields

$$\Gamma_{ev}^{AH-\eta} = \left[ \eta - \left( \frac{5}{2} + \frac{3}{\gamma} \right) \right] e^{-\eta} n_0 \sigma_{el} \bar{v}, \quad (50)$$

while [9] gives

$$\Gamma_{ev}^{AH-\eta} = \eta e^{-\eta} n_0 \sigma_{el} \bar{v}. \quad (51)$$

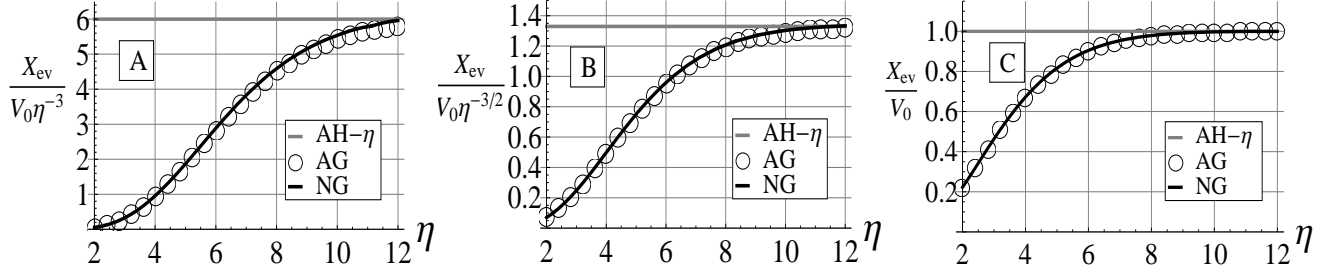


FIG. 5: Plots of  $X_{ev}$  vs  $\eta$  for (A) Linear, (B) Parabolic, and (C) Square potentials.

Thus we get the ratio of  $\Gamma_{ev}^{AH-\eta}$  given in Eq. 50 to those in Eq. 51 for PL trap potentials:

$$\begin{cases} (\eta - 11/2)/\eta, & \text{linear;} \\ (\eta - 4)/\eta, & \text{parabolic;} \\ (\eta - 5/2)/\eta, & \text{square.} \end{cases} \quad (52)$$

Figure 6 compares  $\Gamma_{ev}$ , scaled by  $\eta e^{-\eta} n_0 \sigma_{el} \bar{v}$  in different models. The agreement between NG and AG curves is also satisfying. However, it is obvious that, in Fig. 6 (A) and (B), the AH- $\eta$  curves match the AG ones for  $\eta \gtrsim 8$  and  $\eta \gtrsim 6$  respectively. It is worth emphasizing that the ratios of  $\Gamma_{ev}^{AH-\eta}$  in Eq. 52 only tend to 1 for very

large  $\eta$ .

### F. Elastic Collision Rate Per Atom $\Gamma_{el}$

The elastic collision rate per atom  $\Gamma_{el}$  is defined in Eq. 31

$$\Gamma_{el} = \frac{2}{N} \int_{V_0} d^3r Z(U(\mathbf{r})) = \frac{2A}{V_1 n_0} \int_{V_0} d^3r Z(U(\mathbf{r})), \quad (53)$$

where  $Z(U(\mathbf{r}))$  from Eq. 29 in the AG model can be rewritten as

$$\begin{aligned} Z(U(\mathbf{r})) &= \frac{4n_0^2}{\pi} \sqrt{\frac{2k_B T}{m}} \sigma_{el} \int_0^{\sqrt{\eta}} d\tilde{p}_1 \int_0^{\sqrt{\eta}} d\tilde{p}_2 e^{-(\tilde{p}_1^2 + \tilde{p}_2^2)} \int_0^\pi d\theta_r \sin \theta_r \sqrt{\tilde{p}_1^2 + \tilde{p}_2^2 - 2\tilde{p}_1 \tilde{p}_2 \cos \theta_r} \\ &\times \tilde{p}_1 \tilde{p}_2 e^{-\frac{2U(\mathbf{r})}{k_B T}} \Theta_1 \left[ \eta - \frac{U(\mathbf{r})}{k_B T} - \tilde{p}_1^2 \right] \Theta_2 \left[ \eta - \frac{U(\mathbf{r})}{k_B T} - \tilde{p}_2^2 \right], \end{aligned} \quad (54)$$

with the unitless variables  $\tilde{p}_1 = p_1 / \sqrt{2mk_B T}$  and  $\tilde{p}_2 = p_2 / \sqrt{2mk_B T}$ .

Substituting  $Z(U(\mathbf{r}))$  from Eq. 54 and simplifying the integral with respect to  $\theta_r$ , we can rewrite Eq. 53

$$\begin{aligned} \Gamma_{el}^{AG}(\gamma) &= \frac{32R_0^3 n_0 \sigma_{el} A}{V_1^{AG}(\gamma)} \sqrt{\frac{2k_B T}{m}} \int_0^1 d\tilde{r} \tilde{r}^2 e^{-2\eta \tilde{r}^\gamma} \\ &\times \int_0^{\sqrt{\eta - \eta \tilde{r}^\gamma}} d\tilde{p}_1 \int_0^{\sqrt{\eta - \eta \tilde{r}^\gamma}} d\tilde{p}_2 \frac{\tilde{p}_1 \tilde{p}_2}{3} \\ &\times [(\tilde{p}_1 + \tilde{p}_2)^3 - |\tilde{p}_1 - \tilde{p}_2|^3] e^{-(\tilde{p}_1^2 + \tilde{p}_2^2)}. \end{aligned} \quad (55)$$

We note that the integrand in Eq. 55 is suppressed by  $e^{-2\eta \tilde{r}^\gamma}$  and  $e^{-(\tilde{p}_1^2 + \tilde{p}_2^2)}$ , so the contribution from small  $\tilde{r}$ ,  $\tilde{p}_1$ , and  $\tilde{p}_2$  dominates the integral. Accordingly, in the high- $\eta$  form, the integral can be approximated by extending the upper bound of its interval to infinity. In

addition,  $A$  can be set to unity. Therefore, we have

$$\begin{aligned} \Gamma_{el}^{AH-\eta}(\gamma) &\approx \frac{32R_0^3 n_0 \sigma_{el}}{V_1^{AH-\eta}(\gamma)} \sqrt{\frac{2k_B T}{m}} \int_0^\infty d\tilde{r} \tilde{r}^2 e^{-2\eta \tilde{r}^\gamma} \\ &\times \int_0^\infty d\tilde{p}_1 \int_0^\infty d\tilde{p}_2 \frac{\tilde{p}_1 \tilde{p}_2}{3} \\ &\times [(\tilde{p}_1 + \tilde{p}_2)^3 - |\tilde{p}_1 - \tilde{p}_2|^3] e^{-(\tilde{p}_1^2 + \tilde{p}_2^2)} \\ &= \frac{4\sqrt{2}\pi R_0^3}{V_1^{AH-\eta}(\gamma)} \frac{\Gamma(3/\gamma)}{\gamma(2\eta)^{3/\gamma}} \sigma_{el} \bar{v} n_0 \\ &= \frac{\sqrt{2}}{2^{3/\gamma}} \sigma_{el} \bar{v} n_0, \end{aligned} \quad (56)$$

which is consistent with the high- $\eta$  expressions given in [9]. Here the last equality is obtained by substituting  $V_1^{AH-\eta}$  given by Eq. 39.

The NG integration for  $\Gamma_{el}$  is the most time-intensive of all the calculations. To reduce numerical integration

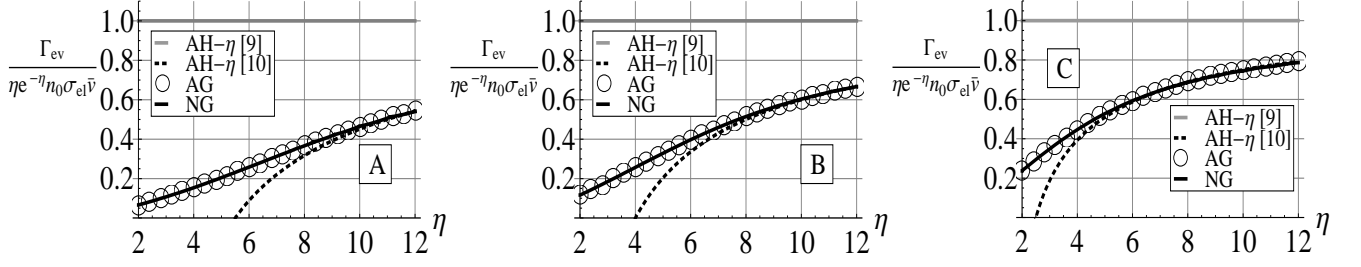


FIG. 6: Plots of  $\Gamma_{ev}$  vs  $\eta$  for (A) Linear, (B) Parabolic, and (C) Square potentials.

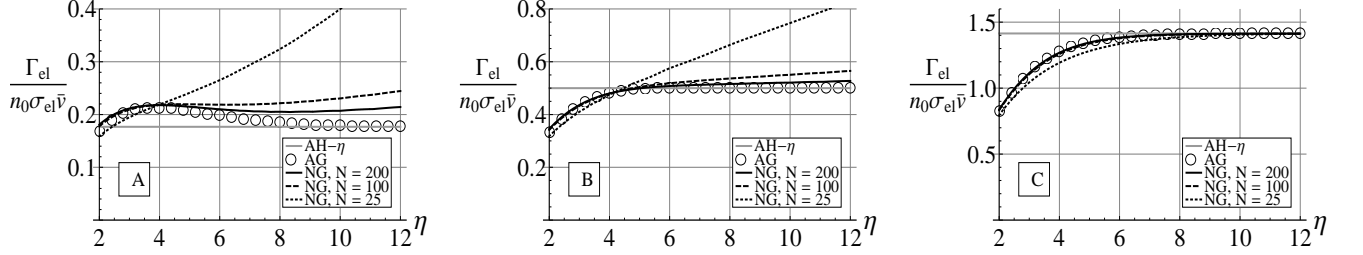


FIG. 7: Plots of  $\Gamma_{el}$  vs  $\eta$  for (A) Linear, (B) Parabolic, and (C) Square potentials with different energy resolution in the numerical integration.

time required to make a lookup table for Eq. 53, we use

$$\rho_{potential}(U) = \int d^3r \delta(U - U(\mathbf{r})) \quad (57)$$

to allows us to evaluate  $Z$  as a function of  $U$ , instead of  $\mathbf{r}$  as

$$\int d^3r Z(U(\mathbf{r})) = \int dU \rho_{potential}(U) Z(U). \quad (58)$$

Then the numerical evaluation of the elastic collision rate is performed as

$$\Gamma_{el} = \frac{2}{N} \int dU \rho_{potential}(U) Z(U). \quad (59)$$

$\Gamma_{el}$  is calculated using a simple constant-step-size rectangle integration method. Interpolating functions for  $Z(U, T)$  and  $\rho_{potential}(U)$  are found by numerically evaluating Eqs. 54 and 57 at discrete sets of  $U$  and  $T$  points and  $U$  points respectively running from 0 to  $\epsilon_t$ . (The  $T$  dependence in  $Z$  is highlighted here for clarity.)

The resolution of the grid of evaluation points used to form the interpolation of  $Z$  was critical. Fig. 7 shows the results for different numbers of points evaluated on each axis ( $T$  and  $U$ )  $N = 25$  (dotted lines), 100 (dashed lines) and 200 (black solid lines) for comparison. The improvement is considerable with more evaluations. However, the computation time varies with  $N^2$ , and it takes about 24 hours to create the  $Z$  interpolating function with  $N = 200$ , which is deemed sufficient given the balance between time and accuracy.

### G. Evaporation Fraction $f$

The evaporation fraction  $f$  is defined in Eq. 28 as

$$f(\eta) = \frac{\Gamma_{ev}}{\Gamma_{el}}. \quad (60)$$

For PL trap potentials, reference [9] gives

$$f^{AH-\eta} = \begin{cases} 4\sqrt{2}\eta e^{-\eta}, & \text{linear;} \\ 2\eta e^{-\eta}, & \text{parabolic;} \\ \eta e^{-\eta}/\sqrt{2}, & \text{square,} \end{cases} \quad (61)$$

which is accurate if  $\eta$  is very high. Improved expressions can be found for high- $\eta$  situations following the treatment of [20]:

$$f^{AH-\eta} = \begin{cases} \frac{2\sqrt{2}[6+2e^\eta(\eta-3)+\eta(4+\eta)]}{-1+e^{2\eta}-2\eta(1+\eta)}, & \text{linear;} \\ \frac{e^\eta\sqrt{2\pi}(2\eta-3)\text{erf}[\sqrt{\eta}]+6\sqrt{2\eta}}{e^{2\eta}\sqrt{2\pi}\text{erf}[\sqrt{2\eta}]-4\sqrt{\eta}}, & \text{parabolic;} \\ \eta e^{-\eta}/\sqrt{2}, & \text{square.} \end{cases} \quad (62)$$

Equation 62 will tend to Eq. 61 with very high  $\eta$ .

In our formalism, which follows the treatment of [10], for the general case, Eq. 60 becomes

$$f^{AG} = \frac{\Gamma_{ev}^{AG}}{\Gamma_{el}^{AG}}, \quad (63)$$

where  $\Gamma_{ev}^{AG}$  and  $\Gamma_{el}^{AG}$  are from Eqs. 49 and 55 respectively. Following our convention, we obtain a third form for the high- $\eta$  approximation by using the high- $\eta$  limits

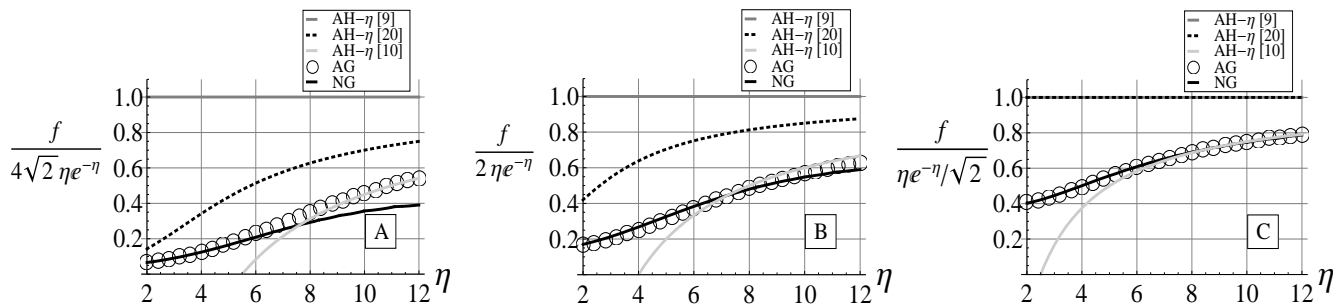


FIG. 8: Plots of  $f$  vs  $\eta$  for (A) Linear, (B) Parabolic, and (C) Square potentials.

for  $\Gamma_{ev}^{AH-\eta}$  and  $\Gamma_{el}^{AH-\eta}$  given by Eqs. 50 and 56 respectively. We arrive at the limiting case that essentially follows from [10]:

$$f^{AH-\eta} = \frac{\Gamma_{ev}^{AH-\eta}}{\Gamma_{el}^{AH-\eta}} = \begin{cases} 4\sqrt{2}(\eta - 4)e^{-\eta}, & \text{linear;} \\ 2(\eta - 11/2)e^{-\eta}, & \text{parabolic;} \\ (\eta - 5/2)e^{-\eta}/\sqrt{2}, & \text{square,} \end{cases} \quad (64)$$

which will also approach Eq. 61 for very high- $\eta$ .

Scaled plots of  $f$  given by different methods are shown in Fig. 8. The discrepancies of  $f$  between AG (circles) and NG results (black solid lines) at high- $\eta$  correspond to discrepancies in  $\Gamma_{el}$  due to the finite resolution of the numerical method as discussed in section IV F. The discrepancies can be reduced, at the cost of time, by increasing the number of sample points when creating the interpolating function of  $Z(U, T)$ . Moreover, although all AH- $\eta$  models give the same results at very high- $\eta$ , care must be taken using approximation expression for  $\eta \lesssim 12$ .

## V. NUMERICAL SOLUTION FOR A REALISTIC TRAP CONFIGURATION

The great advantage of the numerical code is that it can be used for arbitrary trap shapes. This is necessary for our experiments with  $^{88}\text{Sr}$  in an ODT because of the importance of gravity and the small inclination of our trap lasers away from horizontal. For non-ideal traps, it is essential to find an expression for the potential,  $U(\mathbf{r})$ , that describes the potential accurately. We employ an algorithm to find the trap minimum, the trap depth, and the saddle points, which define the trap boundaries and allow us to offset the trap so that the minimum is  $U = 0$ . An example is shown in Fig. 9.

This  $U(\mathbf{r})$  is then passed to the numerical integration routines for statistical mechanical quantities described in Sec. III that are evaluated at a grid of temperature points to construct lookup tables. The lookup tables are used to find interpolating functions for all quantities, which can then be used in place of time-intensive integral evaluations. Using these lookup tables, given initial conditions,

the atom number and temperature evolution can easily be found from Eqs. 23 and 24 using an ordinary differential equations (ODE) solver in *Mathematica*. Typically, one day is needed to create all lookup tables for a given trap potential. After this preparation, a complete ODE solution for several seconds of sample evolution only requires a few seconds of computer evaluation time.

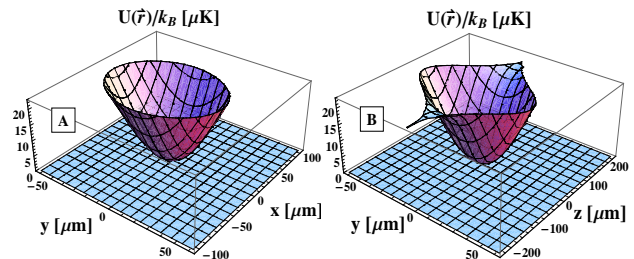


FIG. 9: (Color online) (A) The x-y cut and (B) the y-z cut of the ODT potential for approximately 10 W per beam. The boundary of the trap is the set of points with potential energy equal to the lowest saddle point, which is along the z axis. Gravity is oriented in the  $-\hat{y}$  direction. The beam nearly parallel to the x axis is slightly weaker and less focused than the beam along z, leading to the observed asymmetry.

As described, this procedure is appropriate for a fixed trapping potential. It is possible to form lookup tables that include the variation of ODT laser intensity, or trap depth, and this will allow for changing the potential and modeling of forced evaporation. We are currently working on this improvement.

Figure 10 shows the number and temperature of atoms as functions of time for  $^{88}\text{Sr}$   $^1S_0$  atoms in the ODT. Various quantities such as the one-body loss rate, two-body inelastic collision rate constant, and inelastic cross section can be determined by fitting the calculated evolution curves to experimental data.

We exclude the first few hundred milliseconds from the fit because we expect that atoms are far from equilibrium and significant population is still trapped in the individual beams of the ODT and not in the crossed region at this time. For this fit, we obtain the elastic scattering cross section  $\sigma_{el} = 260 a_0^2$ , one-body loss rate  $\Gamma_1 = 0.3 \text{ s}^{-1}$ , and the ODT photon scattering rate

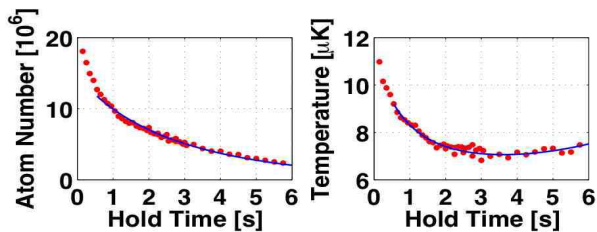


FIG. 10: Variation of atom temperature and number with time for  $^{88}\text{Sr}$  atoms in the  $^1S_0$ . The trap used is described in Fig. 9.

$\Gamma_{ODT} = 0.4\text{s}^{-1}$ . A good fit is found with  $\beta_{in} = 0$  as expected since there are essentially no two-body loss processes in this system.

## VI. ENERGY DEPENDENCE OF THE $^{88}\text{Sr}$ ELASTIC COLLISION CROSS SECTION

Evaporation with an energy-dependent elastic collision cross section has been modeled in [12, 19], but these treatments assume a large cross section that varies because of the unitarity limit. In  $^{88}\text{Sr}$ , the cross section varies because the scattering length is very small, as shown in Fig. 11 [21]. This variation is significant at microkelvin energies, which complicates comparison of theory and experiment because a distribution of collision energies contributes in a thermal sample in the ODT. A full energy-dependent kinetic calculation is beyond the scope of this model. We treat the variation in approximate fashion by assuming the system can be described by an effective, temperature-dependent cross section,  $\langle\sigma_{el}\rangle$ , that is an average of the collision-energy dependent cross section.

To relate  $\langle\sigma_{el}\rangle$  to the underlying energy-dependent  $\sigma_{el}(E_{coll})$ , first consider the standard expression for total collision rate per unit volume in the trapped gas [29, 30]

$$Z(\mathbf{r}) = \frac{1}{2} \int d^3p_1 \int d^3p_2 \sigma_{el} |\mathbf{v}_1 - \mathbf{v}_2| f(\mathbf{r}, \mathbf{p}_1, t) f(\mathbf{r}, \mathbf{p}_2, t). \quad (65)$$

For simplicity, we use untruncated distributions and assume a constant density, which yields

$$Z = \frac{2\pi n_0^2}{\mu} \int dp p^3 \frac{\sigma_{el}(E_{coll})}{(2\pi\mu k_B T)^{3/2}} e^{-\frac{p^2}{2\mu k_B T}}. \quad (66)$$

Here  $\sigma_{el}(E_{coll})$  depends on the collision energy  $E_{coll} = p^2/2\mu$  for  $p = \mu |\mathbf{v}_1 - \mathbf{v}_2|$  and the reduced mass  $\mu = m/2$ . For an energy-independent cross section, this reduces to [29]

$$Z = 2\sigma_{el} n_0^2 \sqrt{\frac{k_B T}{\pi m}}. \quad (67)$$

We assume that the evaporation process is sensitive to an average cross section in which the weighting is taken

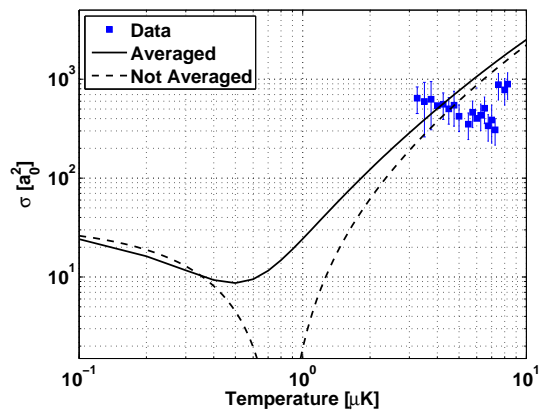


FIG. 11: Measurements and theories for the  $^{88}\text{Sr}$  elastic collision cross section,  $\sigma_{el}$ . The dashed curve is the elastic collision cross section [21] for a collision energy of  $E_{coll} = 2k_B T$ , which is an average collision energy as described in the text. The solid line is an average cross section, weighted by the rate of collisions of a given energy, for the temperature  $T$ .

as the contribution of each collision energy to the total number of collisions per time in the sample. Using this weighting, the average collision energy for a given temperature  $T$  is  $2k_B T$ , and for a given equilibrium temperature, the average cross section is given by

$$\langle\sigma_{el}\rangle = \frac{Z}{2n_0^2 \sqrt{\frac{k_B T}{\pi m}}}, \quad (68)$$

where  $Z$  is calculated using Eq. 66 and the theoretical energy dependence of  $\sigma_{el}$  [21]. Contribution to  $Z$  is not exactly equivalent to contribution to the evaporation rate, but this is a reasonable approximation in the spirit of [12].

Fig. 11 shows variation of  $\sigma_{el}(E_{coll})$  and  $\langle\sigma_{el}\rangle$  for  $^{88}\text{Sr}$  as well as experimental data in which  $\langle\sigma_{el}\rangle$  is extracted using the numerical model. The overall match of the magnitude of the cross section gives confidence in the numerical model. Error bars represent statistical variation. In addition, there is systematic uncertainty due to uncertainty in the trapping potential of typically a factor of two, but this becomes more of an issue for lower sample temperatures and shallower traps, which are more challenging to characterize and model due to the importance of gravity. The assumption of ergodicity may also be less valid at lower temperature because the elastic collision rate and  $\eta$  become very small.

## VII. CONCLUSION

In this paper, we have presented a model describing inelastic and elastic collision dynamics of trapped atoms that can treat traps lacking spatial symmetry and samples with low  $\eta$ . The main assumptions are ergodicity

and a truncated Boltzmann velocity distribution. Statistical mechanical quantities calculated with this numerical model were checked against analytic expressions for power-law traps. This also allowed us to discuss the range of validity of common assumptions made when describing evaporation in power-law traps. The model was also used to describe  $^{88}\text{Sr}$  in an asymmetric ODT with low  $\eta$ , and collisional parameters extracted from the data were found to agree well with theoretical predictions.

## ACKNOWLEDGMENTS

We thank P. Julienne, R. Côté, and P. Pellegrini for helpful discussions and D. Comparat for sharing the original code for describing collisional dynamics of trapped atoms at high  $\eta$ . This work was supported by the Welch Foundation (C-1579), National Science Foundation (PHY-0555639), and the Keck Foundation.

- 
- [1] H. F. Hess, *Phys. Rev. B* **34**, 3476 (1986).
  - [2] T. J. Tommila, *Europhys. Lett.* **2**, 789 (1986).
  - [3] F. Dalfovo, S. Giorgini, L. P. Pitaevskii, and S. Stringari, *Rev. Mod. Phys.* **71**, 463 (1999).
  - [4] S. Giorgini, L. P. Pitaevskii, and S. Stringari, *Rev. Mod. Phys.* **80**, 1215 (2008).
  - [5] E. A. Burt, R. W. Ghrist, C. J. Myatt, M. J. Holland, E. A. Cornell, and C. E. Wieman, *Phys. Rev. Lett.* **79**, 337 (1997).
  - [6] K. M. Jones, E. Tiesinga, P. D. Lett, and P. S. Julienne, *Rev. of Mod. Phys.* **78**, 483 (2006).
  - [7] R. V. Krems, *Int. Rev. Phys. Chem.* **24**, 99 (2005).
  - [8] K. B. Davis, M.-O. Mewes, and W. Ketterle, *Appl. Phys. B* **60**, 155 (1995).
  - [9] W. Ketterle and N. J. van Druten, *Adv. Atom. Mol. Opt. Phys.* **37**, 181 (1996).
  - [10] O. J. Luiten, M. W. Reynolds, and J. T. M. Walraven, *Phys. Rev. A* **53**, 381 (1996).
  - [11] K. Berg-Sørensen, *Phys. Rev. A* **55**, 1281 (1997).
  - [12] P. J. J. Tol, W. Hogervorst, and W. Vassen, *Phys. Rev. A* **70**, 013404 (2004).
  - [13] M. J. Holland, B. DeMarco, and D. S. Jin, *Phys. Rev. A* **61**, 053610 (2000).
  - [14] C. A. Sackett, C. C. Bradley, and R. G. Hulet, *Phys. Rev. A* **55**, 3797 (1997).
  - [15] K. M. O'Hara, M. E. Gehm, S. R. Granade, and J. E. Thomas, *Phys. Rev. A* **64**, 051403 (2001).
  - [16] H. Wu and C. J. Foot, *J. Phys. B* **29**, L321 (1996).
  - [17] Z. Y. Ma, A. M. Thomas, C. J. Foot, and S. L. Cornish, *J. Phys. B* **36**, 3533 (2003).
  - [18] R. Grimm, M. Weidemüller, and Y. B. Ovchinnikov, *Adv. Atom. Mol. Opt. Phys.* **42**, 95 (2000).
  - [19] D. Comparat, A. Fioretti, G. Stern, E. Dimova, B. L. Tolra, and P. Pillet, *Phys. Rev. A* **73**, 043410 (2006).
  - [20] R. deCarvalho and J. Doyle, *Phys. Rev. A* **70**, 053409 (2004).
  - [21] Y. N. M. de Escobar, P. G. Mickelson, P. Pellegrini, S. B. Nagel, A. Traverso, M. Yan, R. Côté, and T. C. Killian, *Phys. Rev. A* **78**, 062708 (2008).
  - [22] S. B. Nagel, C. E. Simien, S. Laha, P. Gupta, V. S. Ashoka, and T. C. Killian, *Phys. Rev. A* **67**, 011401 (2003).
  - [23] S. B. Nagel, P. G. Mickelson, A. D. Saenz, Y. N. Martinez, Y. C. Chen, T. C. Killian, P. Pellegrini, and R. Côté, *Phys. Rev. Lett.* **94**, 083004 (2005).
  - [24] P. G. Mickelson, Y. N. Martinez, A. D. Saenz, S. B. Nagel, Y. C. Chen, T. C. Killian, P. Pellegrini, and R. Cote, *Phys. Rev. Lett.* **95**, 223002 (2005).
  - [25] H. Katori, T. Ido, Y. Isoya, and M. Kuwata-Gonokami, *Phys. Rev. Lett.* **82**, 1116 (1999).
  - [26] J. Ye, H. J. Kimble, and H. Katori, *Science* **320**, 1734 (2008).
  - [27] S. Friebel, C. D'Andrea, J. Walz, M. Weitz, and T. W. Hansch, *Phys. Rev. A* **57**, R20 (1998).
  - [28] W. D. Phillips, in *Proceedings of the International School of Physics Enrico Fermi; course 118, Laser Manipulation of Atoms and Ions*, edited by E. Arimondo, W. Phillips, and F. Strumia (North-Holland, New York, 1992), p. 289.
  - [29] K. Huang, *Statistical Mechanics* (Wiley, New York, 1987).
  - [30] D. A. McQuarrie, *Statistical Mechanics* (University Science Books, Sausalito, 2000).
  - [31] This definition matches Eq. 11 in [20] and Eq. 5 in [9]. Note that  $\lambda$  [9] is equal to  $1/f$  [20] and  $f$  is not the fraction of elastic collision events that result in the evaporation of 1 atom, which is  $2 \times f$ .